RESEARCH ARTICLE | APRIL 10 2023

Efficiency of energy and enstrophy transfers in periodical flows

A. De Leo ; A. Stocchino

Physics of Fluids 35, 046602 (2023)
https://doi.org/10.1063/5.0142848

Physics of Fluids ARTICLE scitation.org/journal/phf

Efficiency of energy and enstrophy transfers in periodical flows

Cite as: Phys. Fluids **35**, 046602 (2023); doi: 10.1063/5.0142848
Submitted: 17 January 2023 · Accepted: 23 March 2023 ·
Published Online: 10 April 2023

A. De Leo[1] and A. Stocchino[2,3,a)]

AFFILIATIONS

[1]Dipartimento di Ingegneria Civile, Chimica e Ambientale (DICCA), Università degli Studi di Genova, 16145 Genova, Italy
[2]Department of Civil and Environmental Engineering, Hong Kong Polytechnic University, Hung Hom, Kowloon 999077, Hong Kong
[3]State Key Laboratory of Marine Pollution, City University of Hong Kong, 83 Tat Chee Avenue, Kowloon 999077, Hong Kong

[a)]**Author to whom correspondence should be addressed:** alessandro.stocchino@polyu.edu.hk

ABSTRACT

We apply a coarse-graining technique to understand the efficiency of scale-to-scale transport of energy and enstrophy in a quasi-two-dimensional weakly turbulent periodic flow. The investigated periodic flow resembles the propagation of a monochromatic tide in a tidal channel, connected to open sea through an inlet. The interaction of the periodic flow with the inlet mouth generates vortical structures in a wide spectrum of scales, and recently, how the corresponding energy and enstrophy fluxes change their signs depending on the tidal phase has been shown. In the present study, we are interested to extend the analysis to the efficiency of the nonlinear transfer rates by analyzing the geometric alignment between the turbulent stresses and the strain rates for the energy, and the vorticity stress and large-scale vorticity gradient for the enstrophy. Our results suggest that, depending on the phase of the period, energy is efficiently transferred to larger scales (inverse cascade) in a finite range of scales, whereas the observed direct energy cascade for very small and very large scales is much less efficient. Enstrophy shows similar behaviors in terms of transitions between direct and inverse cascading; however, all transfers seem to be relatively inefficient.

I. INTRODUCTION

Understanding the energy processes associated with turbulent flows is still a challenging topic that attracts great interest. Turbulence is characterized by a continuum spectrum of flow scales that nonlinearly interact. Classically, the energy transfer among the flow scales is thought of as a cascading process from the wavenumber where energy is injected into wavenumbers where energy is dissipated. The direct cascade is described by the Kolmogorov $-5/3$ power law in the inertial range. However, the existence of several energy and enstrophy cascades have been shown starting from experimental measurements or numerical simulations, especially for two-dimensional or quasi-two-dimensional turbulent flows.[1] Moreover, flow inhomogeneities, coherent vortices, and two-dimensionality proved to force different scales, and, in some cases, different power laws can be detected, depending on the range of wavenumbers considered.[1] Coherent structures are indeed able to control the overall energy transfers as recently reported by Thiesset and Danaila.[2] Restricting our attention to 2D dimensional or quasi-2D dimensional turbulence, the two relevant global inviscid invariants are the kinetic energy and the enstrophy, the budget of which can be regulated by several concurring processes that ultimately can be expressed in terms of direct or inverse cascades. Turbulent energy fluxes can be associated with the action of stresses, arising from the exchange of momentum between scales owing to the nonlinearity in the Navier–Stokes equations, against the rate of strain. Similarly, enstrophy transfer rates are governed by "stresses" and vorticity gradients. The study of the energy and enstrophy fluxes in two-dimensional turbulence has received great attention, taking advantages of new frameworks that allow for a scale-to-scale analysis, namely coarse-graining techniques.[3–5] Coarse-graining methods, which is different from spectral methods in Fourier space, retain the energy/enstrophy transfers in space and can be applied to inhomogeneous flows.[3,4,6–9] Successful applications of coarse-graining methods are found in several studies of turbulent or turbulent-like flows in two-dimensional applications.[9–18] Most of the cited works focused on the description and interpretation of the nonlinear energy and enstrophy fluxes in relatively idealized systems, e.g., flows of thin layers or numerical simulations of 3D homogeneous turbulence. The physical mechanisms behind the energy and enstrophy cascades in the context of inverse energy cascades have been suggested in two important

contributions,[10,11] and the proposed interpretation have been proved several times since then. Relevant for the present analysis is the introduction of the concept of energy efficiency discussed by Fang and Ouellette,[9] where the authors considered the conditional statistics of the alignment of the stress and the strain rate. In particular, the efficiency of the nonlinear fluxes was defined as the cosine of twice the angle between the eigenvectors corresponding to the highest eigenvalue of the (deviatoric) stress and strain rate. They concluded that advection tends to disrupt the delicate geometric balance that is required to transfer energy from scale to scale, causing a reduction in the efficiency of the turbulent cascade. They suggested that a careful investigation of the efficiency of the energy transfer should complement the analysis of the signs of the nonlinear fluxes, which, by themselves, cannot provide a clear indication of whether the cascade processes efficiently occur or not.

The application of the above theories on energy and enstrophy cascading in geophysical contexts poses several challenges, most of them related to the large scales of the domain involved, the simultaneous presence of different forcing of the dynamics (tides, waves, wind current, baroclinic currents), and the complex geometry. However, estimating the energy budget and fluxes in ocean is of paramount importance, and several studies related to this can be found in the recent literature.[5,19–23] Most of the studies pertain to energy budget in open ocean, where both direct and inverse cascades have been identified depending on the local characteristics of the flow. However, much less has been done in coastal areas, where tidal flows can dominate.[24] In fact, high energy tidal currents, interacting with coastlines, generally induce the development of quasi-2D coastal tidal vortices, the importance of which for momentum, mass, and energy transport is well recognized.[25–32] Moreover, coastal areas are characterized by the most energetic currents induced by different forcing sources, such as tides and waves. Moreover, the interaction of these currents with complex shorelines (headlands, islands, tidal inlets, and coastal bays) triggers the generation of vortical structures at several scales. Due to the shallowness of the coastal areas, the flow can be safely regarded as quasi-two-dimensional, and the typical macro-vortices can be regarded as two-dimensional flow structures.[33,34] Several studies have been devoted to understand the importance of tidal pumping and tidal macro-vortices as a primary agent of dispersion.[35,36] However, the influence of tidal induced macro-vortices on energy and enstrophy cascades has been less investigated, and it is the main focus of the present analysis. In recent contributions,[37–39] the authors performed a series of experiments on a large tidal flume, varying the forcing tidal wave. Time resolved high-resolution velocity fields were measured using particle image velocimetry. Coarse-graining method was applied to quasi-2D velocity fields revealing a variety of energy/enstrophy cascading scenarios depending on the tidal phase. Both inverse and direct energy/enstrophy cascades were observed and associated with vortex merging and thinning,[11,12] and the predominance of straining has been recalled[10] especially in the ebb phase of the tide.

Starting from the above analysis, we focus on the efficiency of the transfer rates. In fact, the computation of the nonlinear fluxes using the coarse-graining techniques has been shown to be accurate not only for determining the sign of the fluxes but also for computing the efficiency of the process.[9,15] Following a similar analysis as described in the cited contributions, we intend to investigate the efficiency of the multiple cascading observed in the experiments discussed in De Leo and Stocchino.[37] The present contribution represents the first study dedicated to the analysis of the energy and enstrophy efficiency transport of coastal tidal flows.

II. MATERIAL AND METHODS

A. The experimental dataset

In the present analysis, we used the 2D velocity dataset measured during a series of experiments discussed in detail by De Leo and Stocchino.[37] Herein, we briefly recall the main characteristics of the large-scale experimental flume, the forcing tidal wave, and the measuring technique.

The flume consisted of two main parts: a compound tidal channel (23 m long) and a rectangular basin representing the open sea (about 6 m long). The basin is connected to the tidal channel through an inlet composed of two vertical barriers with dimension $l_w = 0.86$ m and a net entrance width of $w_i = 0.7$ m. The geometry of the tidal channel was designed to reproduce a compound cross section, composed of a deep main channel and wide lateral tidal flats. The flow generated by a volume wave generator, placed at the extreme end of the basin, was forced to enter the channel through the tidal inlet. The main channel longitudinal slope is equal to 0.255%. The outer basin is 6 m long and 2.20 m wide (w_b), with a maximum depth equal to $h_b = 0.5$ m and a horizontal bottom. The mean water elevation referred to as the bottom of the channel at the channel inlet (D_0) has been maintained constant and equal to 0.36 m during all experiments. The surface of the entire experimental apparatus is finished in concrete and the estimated Chézy conductance coefficient C is about 10 $m^{1/2}/s$. To provide an oscillating water level, a tidal generator system (oscillating cylinder) has been installed at the end of the rectangular basin. The cylinder is remotely controlled using a digital signal acquisition/generation system, and it provides a time law signal of the kind as follows:

$$\eta = a \sin(\omega t), \tag{1}$$

where t is the time, η is the free surface elevation, a is the tidal amplitude, and $\omega = 2\pi/T$ is the tidal angular frequency, T being the tidal period. A sketch of the apparatus is given in Fig. 1.

The present case of periodic flows is intended to mimic realistic tidal wave conditions. To this end, we decided to follow Toffolon *et al.*[40] for the main parameters governing the hydrodynamics of monochromatic tidal waves. In particular, the friction parameter (χ) is known to play an important role and it is defined as

$$\chi = \epsilon \frac{L_g}{2\pi C^2 D_0}, \quad \text{with} \quad L_g = T\sqrt{gD_0}, \tag{2}$$

where D_0 is the mean flow depth, and L_g is the inviscid tidal wavelength. We designed the present experiments preserving the friction parameter χ, i.e., selecting appropriate values of the tidal waves (amplitude and period) to reproduce realistic values of the friction parameter. Moreover, the Froude number, defined as $F_r = U/\sqrt{gD_0}$, with g as the gravity acceleration, is naturally preserved between the real world and the laboratory model for a prescribed value of χ. Table I reports the main experimental parameters.

During each experiment, the water level and surface velocities have been measured. In particular, free surface elevation was monitored using four ultrasound gauges placed at a distance of 0, 4.75, 14.3, and 25 m from the tidal wave maker.

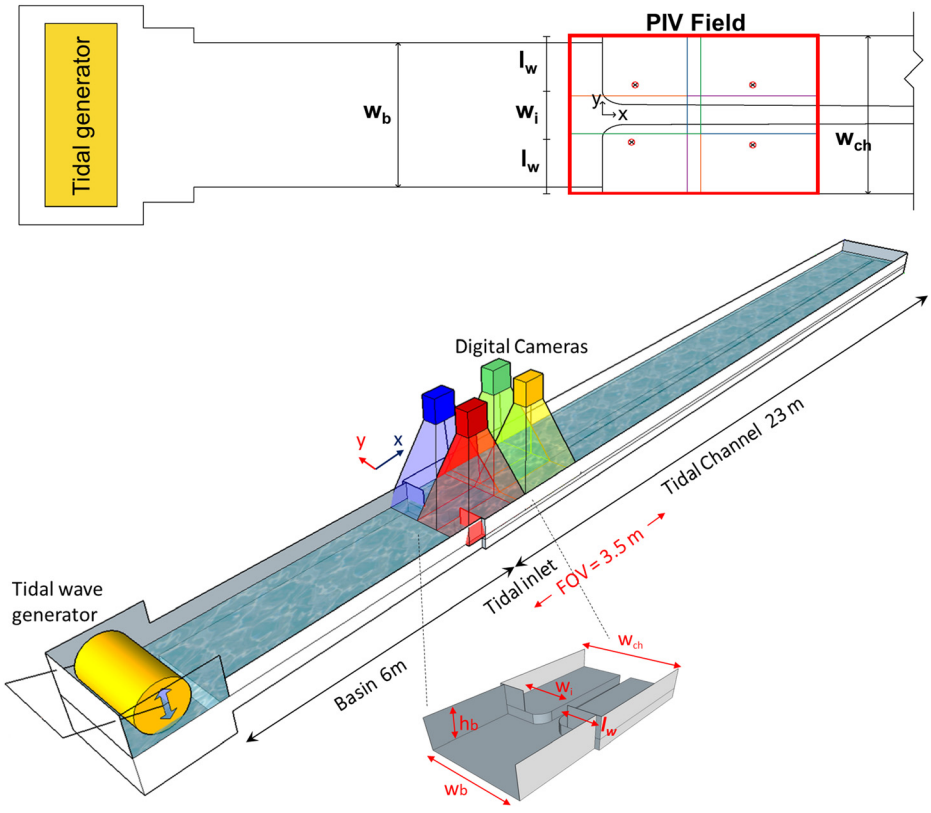

FIG. 1. Sketch of the experimental setup. The area of measurements of PIV is shown as a red rectangle in the plan view of the experimental channel (top figure).

Time resolved high-resolution surface velocity fields $\mathbf{u}(\boldsymbol{x}, t) = (u(\boldsymbol{x}, t), v(\boldsymbol{x}, t))$ were measured using particle image velocimetry (PIV) and constitutes the dataset for the present analysis. Lighting was produced using eight 500 W white light halogen lamps. The channel water surface was densely and uniformly seeded by polyethylene particles (dimension of about 3 mm) used as PIV tracers. PIV acquisitions were recorded employing four high-resolution GigaEthernet digital camera (Teledyne Dalsa Genie Nano C1280, resolution 1280×1024 pixels). Cameras were fixed on rigid supports placed at an elevation of 2.5 m from the bottom of the channel, pointing downward, as shown in Fig. 1. Based on the camera arrangement, the field of view (FoV) for the velocity measurements was positioned to cover an area of about 3.5×2.5 m^2. In the top panel of Fig. 1, the area of measurements is indicated with a red rectangle. We covered the entire width of the channel, and the dimension in the longitudinal direction was enough to register the most important processes around the inlet. The PIV acquisition frame rate was set equal to 20 fps. For each set of parameters (T and ϵ), we repeated the experiments ten times for a single period. The images from the four digital cameras have been binarized and then merged to obtain single panoramic images of the entire FoV for each temporal instant before the PIV analysis. Based on this configuration, the smallest scale resolved was around 2 cm. For the present analysis, the dynamic range of the PIV, defined as the ratio of the maximum to the minimum resolvable displacement,[41,42] was wide enough to resolve the velocity scales at hand. In fact, different from the standard PIV based on the analysis of two frames separated by a short laser pulse, we continuously recorded the particle displacement with a frequency high enough to sufficiently capture the fastest flows. After, optimizing the image stride, the PIV processing was adapted to increase the dynamic range.

TABLE I. Experimental forcing tide parameters.

exp.HR	ϵ	T (s)	L_g (m)	R_e	χ	F_r
01HR	0.0325	180	195.3	16 850	0.12	0.04
02HR	0.0308	160	173.6	21 500	0.11	0.05
03HR	0.0225	130	141.0	24 800	0.065	0.07
04HR	0.0217	100	108.5	31 600	0.033	0.08

B. Coarse-grain method for nonlinear energy and enstrophy transfer rates

The approach we used in the present study for analyzing the spatial and temporal variability of the nonlinear energy and enstrophy fluxes is based on the so-called coarse-graining technique, first introduced in turbulence flow studies in the framework of large eddy simulation.[3] The main idea is to build low-pass spectral filtered velocity fields by convolving the flow fields with a filter function $G_l(\boldsymbol{x})$ with a cutoff length l. Thus, flow scales smaller than l are suppressed and larger scales are preserved. Different filtered fields are then obtained as a function of the cutoff length l.[6–9,13–16] Several choices have been

proposed for the filter function $G_l(\boldsymbol{x})$, such as top-hat or Gaussian filter among others, all characterized by a fast decay in space.[16] For the present analysis, we used a top-hat filter of the following kind:

$$G_l(x) = \begin{cases} 1 & x < l, \\ 0 & \text{otherwise.} \end{cases} \tag{3}$$

The coarse-grained equation for the mean kinetic energy at the scale l, $E^{(l)}$ is then obtained in the following form:[8,43]

$$\frac{\partial E^{(l)}}{\partial t} + \frac{\partial J_i^{(l)}}{\partial x_i} = -\Pi^{(l)} - \nu \frac{\partial u_i^{(l)}}{\partial x_j}\frac{\partial u_i^{(l)}}{\partial x_j} - \alpha |\boldsymbol{u}^{(l)}|^2, \tag{4}$$

where $\boldsymbol{J}$ synthetically collects all transport terms, $\Pi^{(l)}$ is the new term arising from the coarse-graining, the second term on the right hand side is the energy dissipation, and the last term represents the large-scale dissipation due to friction. $\boldsymbol{J}$ only acts to redistribute the energy in space, and it is not involved in the transfer of energy across scales.

The nonlinear energy flux $\Pi^{(l)}$ is responsible for the redistribution of energy across scales and appears in the equation for mean kinetic energy at the scale l ($E^{(l)}$), and it is defined as follows:

$$\Pi^{(l)}(x, y, t) = -\tau_{ij}^{(l)}(x, y, t) S_{ij}^{(l)}(x, y, t), \tag{5}$$

where $\tau_{ij}^{(l)} = (u_i u_j)^{(l)} - u_i^{(l)} u_j^{(l)}$ is the residual stress tensor, and $S_{ij}^{(l)} = 1/2(\partial u_i^{(l)}/\partial x_j + \partial u_j^{(l)}/\partial x_i)$ is the filtered rate of strain.[11,12,15] The term $\Pi^{(l)}$ links the filtered small scales and the resolved large flow scale. In particular, $\Pi^{(l)} > 0$ implies energy transfer to smaller scales and, conversely, $\Pi^{(l)} < 0$ denotes energy transfer toward larger scales.

A similar decomposition can be applied to the enstrophy budget leading to the definition of the coarse-grained enstrophy flux as follows:[16]

$$Z^{(l)}(x, y, t) = -\sigma_i^{(l)}(x, y, t) \frac{\partial \omega^{(l)}(x, y, t)}{\partial x_i}, \tag{6}$$

where $\omega^{(l)}$ is the vorticity (in this case, the out-of-plane component), and $\sigma_i^{(l)} = (u_i \omega)^{(l)} - u_i^{(l)} \omega^{(l)}$ is the vorticity stress. The same sign convention holds for the enstrophy fluxes $Z^{(l)}$.

Crucial for the present analysis is the fact that Eq. (5) expresses $\Pi^{(l)}$ as the inner product between the residual stress and the filtered rate of strain,[12,44] and this allows for rewriting $\Pi^{(l)}$ as

$$\Pi^{(l)} = -2\lambda_\tau^{(l)} \lambda_S^{(l)} \cos(2\Theta_\Pi), \tag{7}$$

where $\lambda_\tau^{(l)}$ is the maximum eigenvalue of the deviatoric part of $\tau_{ij}^{(l)}$, $\lambda_S^{(l)}$ is the maximum eigenvalue of rate of strain tensor, and Θ_Π is the angle between the corresponding eigenvectors. Following the same approach, the enstrophy flux can be computed in terms of the product between the moduli of the vorticity stress $|\boldsymbol{\sigma}^{(l)}|$ and of the vorticity gradient $|\nabla \boldsymbol{\omega}^{(l)}|$, and the angle between the vectors Θ_Z (Refs. 9 and 15) as

$$Z^{(l)} = -|\boldsymbol{\sigma}^{(l)}||\nabla \boldsymbol{\omega}^{(l)}| \cos(\Theta_Z). \tag{8}$$

Equation (7) shows how the transfer is linked to the alignment between the eigenframes of $\tau_{ij}^{(l)}$ and $S_{ij}^{(l)}$. The term $\cos(2\Theta_\Pi)$ describes the efficiency of the energy transfers through the different flow scales, providing an estimate of the fraction of the turbulent stress that works against the large-scale strain.[9,15,45] A perfect misalignment ($\Theta_\Pi = \pi/4$) between stress and strain prevents the energy transfers, leading to a zero efficiency. The energy transfer has the maximum efficiency for $\Theta_\Pi = \pi/2$ toward the small scales (the stress aligns perfectly with the compressive strain-rate eigenvector) and for $\Theta_\Pi = 0$ toward the larger scales (perfect alignment). The discriminant value of Θ_Z is $\pi/2$, but similar considerations can be provided.

The computation of the energy and enstrophy fluxes, both using the original definitions, Eqs. (5) and (6), and the decomposition expressed as Eqs. (7) and (8), has been performed as in the study by De Leo and Stocchino[37] for the boundary treatment and the computation of the time and space averages.

In fact, care must be taken to avoid spurious effects owing to the finite size of the domain and the possible interaction with the largest separation adopted for the filtering functions. For the present study, we have started from the discussion presented in Rivera *et al.*[16] and Aluie *et al.*[5] regarding the treatment of boundaries. As known, the errors might arise at Kernel sizes larger than the domain size. In the present study, the domain has very different dimensions along the two axes, i.e., the longitudinal size of the tidal channel is about ten times its width. Among the strategies discussed in the cited works, we followed the approach suggested in Aluie *et al.*[5] that coupled with the top-hat filter, more localized in space compared to the Gaussian, allowed for producing reliable estimates of the fluxes up to a non-dimensional scale l/l_w around 4. For larger separations, the quality of the results rapidly decreased.

Finally, the study of energy cascades classically relies on standard methods based on Fourier analysis.[19,22,46] On the one hand, Fourier spectral analysis provides important results in term of energy spectra; on the other hand, it has a limited applicability to quasi-homogeneous regions with simple boundary conditions, and the technique typically needs some kind of special treatment at the boundaries. Since the application of Fourier analysis requires homogeneity of the flow fields, for the present analysis, we preferred to apply coarse-graining that, in turn, correctly retains the non-homogeneous character of the nonlinear transfers.

C. On the applicability of the shallow water hypothesis

Equation (4) is strictly valid for two-dimensional incompressible turbulence, and its extension to the three dimensional case has been recently discussed by Ballouz and Ouellette.[44]

Turbulent flows are in general always three dimensional. However, as discussed in several reviews dedicated to two-dimensional turbulent flows, the dimension of the problem can be reduced by constraining the development of the flow in one spatial direction. To this end, imposing a geometric anisotropy among the three dimension and, in particular, strongly reducing the flow in one of the three direction is an efficient way to produce a two-dimensional or quasi-2D turbulent flow.[47–49]

Thus, the so-called shallow water approximation is usually assumed to be valid in many geophysical flows, based on the large-scale separation between the vertical and horizontal dimensions, i.e., the ratio δ between the typical vertical length scale (water depth, D_0) and the typical horizontal length scale (L) is much less than unity. In fact, starting from the 3D Reynolds equation

$$\rho \frac{\mathrm{d}u_i}{\mathrm{d}t} = \rho f_i - \frac{\partial P}{\partial x_i} + \mu \frac{\partial^2 u_i}{\partial x_j^2} - \frac{\partial \left(\rho \langle v_i' v_j' \rangle \right)}{\partial x_j}, \tag{9}$$

we focus the discussion on the relative importance of the terms in the vertical component

$$\frac{\partial w}{\partial t} + u\frac{\partial w}{\partial x} + v\frac{\partial w}{\partial y} + w\frac{\partial w}{\partial z} = \frac{1}{\rho}\frac{\partial P}{\partial z} + g\cos\theta - \frac{\partial \langle w'u' \rangle}{\partial x} - \frac{\partial \langle w'v' \rangle}{\partial y} - \frac{\partial \langle w'w' \rangle}{\partial z}. \tag{10}$$

We set U_0 as the typical velocity scale for u and v, and ΔU_0 for their variations, which is at most of the order of U_0. The continuity equation shows that the vertical velocity is of order $O(\delta \Delta U_0)$, which is much smaller than ΔU_0. The momentum equation along the vertical direction can be simplified into the hydrostatic pressure distribution provided that two conditions are satisfied. First, the non-dimensional group $F_r^2 \delta^2$ must be less than 1, with F_r being a typical Froude number. The latter implies that the convective terms in the vertical momentum equation are negligible with respect to the gravitational term. Second, the non-dimensional group $F_r^2 \delta / C$, where C is a Chézy coefficient assuming a closure of the turbulent stress in terms of an eddy viscosity, must be less than 10, i.e., the gravitational term is much greater than the divergence of the Reynolds stresses.

For the present experiments, the ratio between the typical vertical length scale (water depth) and the typical horizontal length scale (channel width) is about $\delta = 10^{-2}$. Based on the length and velocity scales of the experiments, the two non-dimensional groups are of the order of about 10^{-5}. Thus, we expect that the resulting velocity fields are substantially two-dimensional, with residual three dimensional effects limited to small regions close to the channel bottom or around the edges of the tidal inlet. In this case, Eq. (4) can be considered valid for the present investigation, similar to many other studies regarding shallow layers of fluids.[9,13–16]

III. RESULTS AND DISCUSSION

A. The periodic flow fields

The description of the flow under investigation has been provided in recent contribution by the authors, both in terms of Eulerian and Lagrangian properties, and we refer to these contributions for the details.[37–39] Herein, we briefly summarize the main features that will help the discussion of the present results. The volume wave, generated by the periodic oscillation of the tidal generator, propagates toward the tidal channel with a wavelength L_g much longer of the channel length. The resulting flow remains relatively regular until it interacts with the tidal inlet during the flood phase, i.e., when the mean flow intrudes in the tidal channel directed to the positive x. As soon as the almost uniform flow approaches with the lateral thin barriers, vortex shedding is observed from the tips of the two plates. A series of small-scale vortices are continuously emitted during the flood phase and tend to merge in a larger recirculating structure that, ultimately, occupies the entire lateral flat at the peak of the flood. Nicolau del Roure *et al.*[25] already described the entrainment of small-scale vortices in the main vortical structure, and De Leo *et al.*[38] reinterpreted this process in terms of Lagrangian-averaged vorticity deviation (LAVD)[50] and finite time Lyapunov exponent dynamics.[51–54]

Particularly relevant for the present study is the Lagrangian-averaged vorticity deviation (LAVD), defined as[51]

$$\mathrm{LAVD}(t_1, t_0, \boldsymbol{x_0}) = \int_{t_0}^{t_1} |\boldsymbol{\omega}(\boldsymbol{x}(s, \boldsymbol{x_0}), s) - \bar{\boldsymbol{\omega}}| ds, \tag{11}$$

where $\bar{\boldsymbol{\omega}}$ is the spatial mean of vorticity.

The inversion of the mean flow during the ebb phase of the tidal wave (mean flow directed toward the outer basin) causes the disruption of large gyres and, ultimately, the large-scale flow tends to completely flush the macro-vortices out of the tidal channel. The observed asymmetry between the vortex shedding at the inlet during the flood and the ebb phase is attributed to the geometry of the channel (compound cross section) and of the basin (rectangular cross section).[39] On the contrary, the symmetry of the inlet and tidal channel with respect to the x axis imposes a symmetry in the flow along the transverse direction. In the present experiments, the typical Strouhal number,[25] defined as $S_t = L/UT$, where L is a typical length scale related to the vortex shedding generation set equal to l_w, U is a convective velocity scale, and T is the tidal period, assumes values in a range between 0.07 and 0.08, which is in line with previous experimental studies[25] and field applications.[32] In fact, vortex shedding is observed with a period much shorter than the tidal period. LAVD fields showed that small coherent patches are generated at the tip of the tidal inlet and, following them by advecting the LAVD fields, these patches tends to produce elongated and thinned filaments immersed in the large-scale gyres on the lateral tidal flats.[38] Due to the longitudinal symmetry of the channel, this process is identical on the two sides of the tidal channel. A visualization of the LAVD fields computed for three tidal periods is shown in movie 2 (Fig. 2, Multimedia view), together with the velocity recorded in one point at the tidal inlet. From the movie, the process of vorticity shedding at the tip of the tidal barrier appears neatly. Periodic emissions of patches of LAVD are then convected by the mean flow toward the tidal channel, during flood phase (when the velocity at the inlet is positive). During ebb phase (negative velocities at the inlet), large regions with high values of LAVD are destroyed and transported away from the channel toward the open basin.

Finally, the observations and measurements indicate that the large-scale gyres have horizontal dimensions about an order of magnitude larger than the flow depth, confirming the validity of the assumptions described in Sec. II C. Regarding the presence of possible secondary flows triggered by the inlet barrier and the compound geometry, similar to many other contexts, their role is mainly restricted to very small scales close to the bottom corners. Considering a free surface flow in straight uniform condition with or without a compound geometry as 2D or quasi-2D is a standard assumption in theoretical and experimental studies of this field.[55–62]

B. Spatial distribution of energy and enstrophy transfer rates

We are now interested in studying how the periodical evolution of the large-scale flow together with the observed generation/destruction of coherent vortical structures at different scales influence the energy and enstrophy transfer rates among the scales. Vortex merging/thinning is known to be responsible for a possible establishment of an inverse energy cascade,[11,12] and the presence of coherent vortices might sustain energy cascades even for relatively low Reynolds

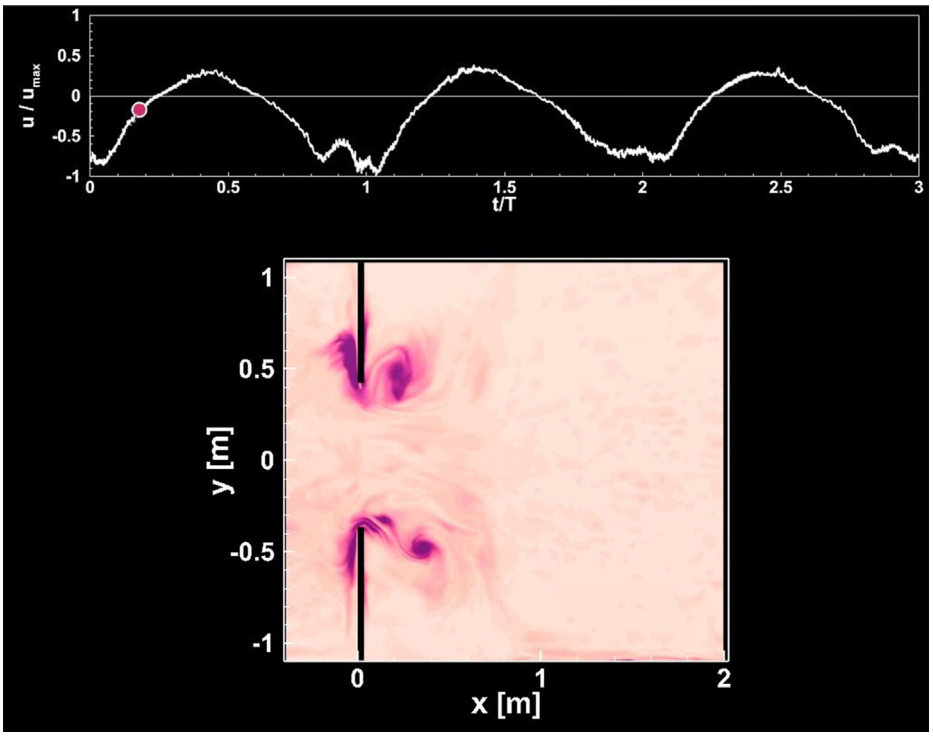

FIG. 2. Snapshot of the time evolution of the LAVD fields of experiment HR04 together with the longitudinal velocity normalized with the peak tidal velocity recorded in the center of the tidal inlet. Multimedia view: https://doi.org/10.1063/5.0142848.1

numbers.[2] The true potential of the coarse-grain method is to retain the temporal and spatial distribution of the fluxes, revealing their variability in space and time. Examples of the spatial distribution of $\Pi^{(l)}(\boldsymbol{x})$ and $Z^{(l)}(\boldsymbol{x})$ computed using Eqs. (7) and (8) are shown in Fig. 3 together with the corresponding velocity fields of the most energetic experiment (04HR). In this example, we show the results obtained for a separation $l/l_w \cong 1$. Contours of the swirling strength λ_{ci} are reported in the figure superimposed on the vector velocity fields. Swirling strength is defined as the positive imaginary eigenvalue of the local velocity gradient tensor and shows high values where there is a strong local flow rotation, i.e., a vortex.[63] In the present context, we employed the computation of λ_{ci} to help the identification of vortical structures embedded in the flow.

Panel (a) shows an instantaneous velocity field observed at the peak of the flood phase, i.e., corresponding to the maximum velocities toward the tidal channel. The selected instant is representative of the situation where coherent vertical structures are observed at different scales, from small vortices with a typical size of a portion of l_w up to the large-scale gyres that occupy the entire lateral expansion of the channel, see Fig. 9 of De Leo *et al.*[38] Panels (c) and (d) report the corresponding computed energy and enstrophy fluxes, respectively. Both velocity and the nonlinear flux ($\Pi^{(l)}(\boldsymbol{x})$ and $Z^{(l)}(\boldsymbol{x})$) fields appear to be symmetrical along the y axis, and the energy fluxes show positive (indicating a transfer to smaller l) and negative spots (indicating a transfer to larger l). Intense negative values are observed in the proximity of the inlet where the vortices are shed and then thinned, whereas positive values are concentrated far from the inlet. In the latter region, the flow is almost uniform, and it is not surprising that the energy flux indicates the presence of a direct energy cascade. The enstrophy flux shows high positive values at the inlet, whereas a large area of negative values is observed between $x = 1$ and $x = 1.5$ m, approximately.

During the ebb phase, i.e., the flow is mainly directed from the channel to the outer basin, see panel (b) for an example of the velocity field; the behavior of $\Pi^{(l)}(\boldsymbol{x})$ and $Z^{(l)}(\boldsymbol{x})$ is quite different from the flood phase, see panels (d) and (f), respectively. The energy flux [panel (d)] is almost everywhere positive with higher values around the tidal inlet. Similarly, the enstrophy flux is dominated by positive values, and it is stronger around the inlet.

In general, this behavior has been observed for all experiments regardless of the forcing tidal wave with some differences related to the intensity of the flux and the spatial distribution of the positive and negative patches. In fact, as described in De Leo *et al.*,[39] the pattern of the flow structures is quite similar, varying both the amplitude and the wavelength of the tidal waves; decreasing the wavelength of the forcing monochromatic tide generates intense flows, and, ultimately, the dimensions of the lateral macro-vortices increase in the longitudinal direction.

C. Time and spatial averaged energy and enstrophy fluxes

We now evaluate the spatiotemporal averages of the transfer rates $\langle \Pi^{(l)} \rangle$ and $\langle Z^{(l)} \rangle$ that are usually adopted to interpret the overall scenarios in terms of energy cascades (see Refs. 9, 45, and 64, among others). We could expect to find constant negative (positive) values of $\langle \Pi^{(l)} \rangle$ in the inertial range of the inverse (direct) energy cascade, and zero everywhere else. On the contrary, a split-energy cascade is characterized by a positive nonlinear energy flux for scales smaller than the injection scale and negative flux for

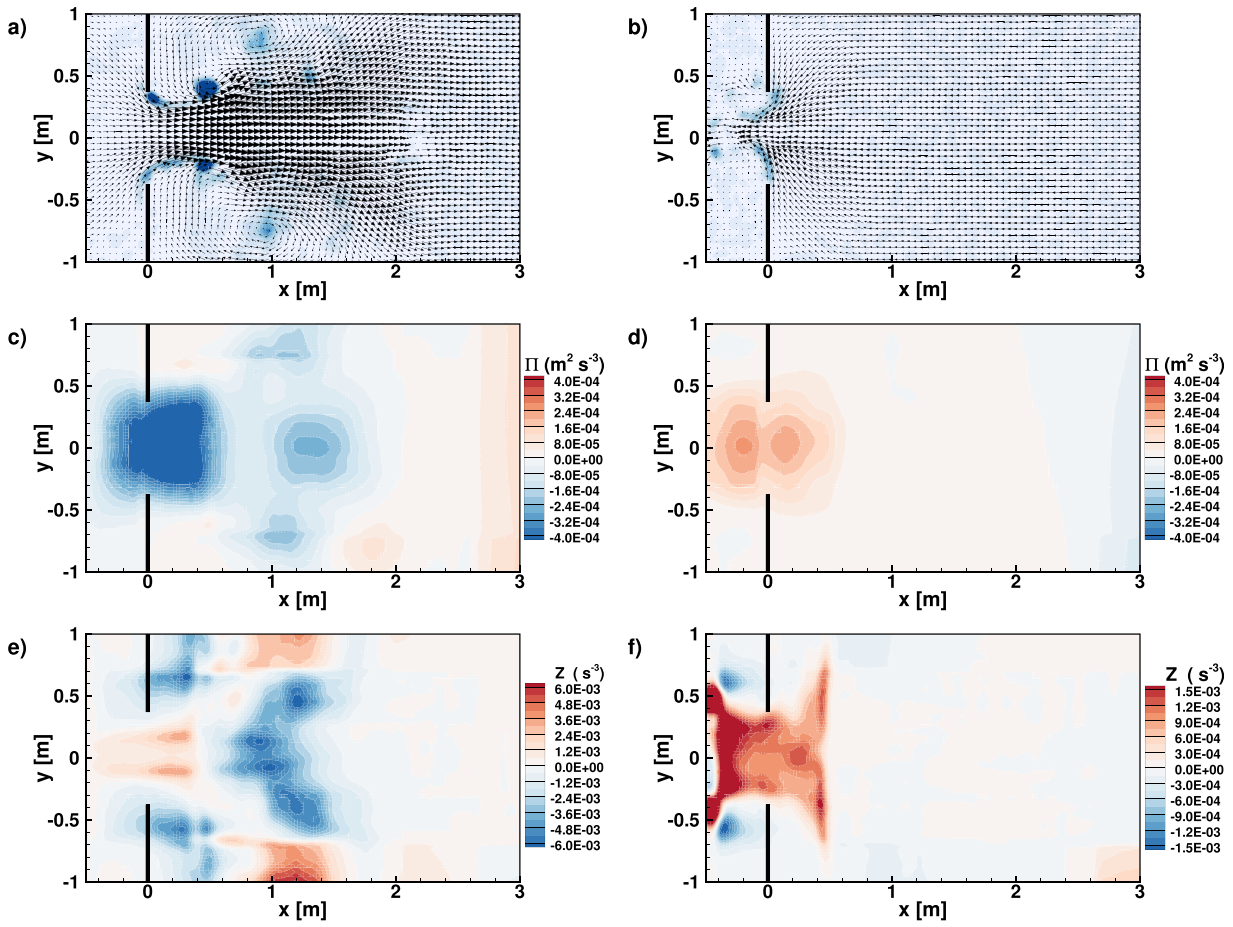

FIG. 3. Snapshots of the measured velocity fields together with the contours of the swirling strength and spatial distribution of the energy fluxes $\Pi^{(l)}$ and enstrophy fluxes $Z^{(l)}$ for a separation $l/l_w \cong 1$ for experiment 04HR. (a) Velocity field at the maximum flood ($t = T/4$); (b) velocity field at the maximum ebb ($t = 3T/4$); (c) field of $\Pi^{(l)}(\boldsymbol{x})$ at $t = T/4$; (d) field of $\Pi^{(l)}(\boldsymbol{x})$ at $t = 3T/4$; (e) field of $Z^{(l)}(\boldsymbol{x})$ at $t = T/4$; and (f) field of $Z^{(l)}(\boldsymbol{x})$ at $t = 3T/4$.

scales larger than the injection scale. Differently from previous studies on turbulent-like flows (e.g., Refs. 9 and 45), we followed the approach described in De Leo and Stocchino[37] to characterize the process during the different phase of the period. The results in terms of spatiotemporal averaged fluxes $\langle\Pi^{(l)}\rangle$ and $\langle Z^{(l)}\rangle$ are shown in Fig. 4 for all experiments.

As discussed by De Leo and Stocchino,[37] for all experiments, we observed a symmetric behavior of $\langle\Pi^{(l)}\rangle$ as a function of the separation l/l_w if we consider flood and ebb phase, green and blue lines, respectively. During flood, $\langle\Pi^{(l)}\rangle$ is strongly negative in a range of scales between $l/l_w \cong 0.16$ and $l/l_w \cong 2 - 2.5$, denoting an inverse transfer. A small range of direct energy transfer is found for $l/l_w \lesssim 0.16$. An opposite scenario occurs during ebb, when the macrovortices are flushed-out from the channel by the reversing flow. In fact, $\langle\Pi^{(l)}\rangle$ is positive (direct energy transfer) for $l/l_w \gtrsim 0.16$. The transition between the flood-type to the ebb-type scenario occurs smoothly, considering $\langle\Pi^{(l)}\rangle$ for all times, not shown here. The minimum (maximum) value of $\langle\Pi^{(l)}\rangle$ during flood (ebb) is always found to be at a separation approximately equal to 1, and the corresponding spatial distributions of $\Pi^{(l)}$ are shown in Fig. 3.

Averaging over the entire period lead to a distribution of $\langle\Pi^{(l)}\rangle$ (red lines) similar to the one obtained during flood.

The spatiotemporal averaged enstrophy over the period is shown as a black line in Fig. 4. $\langle Z^{(l)}\rangle$ is strongly positive for $l/l_w \lesssim 0.16$ and negative for larger scales. The signs of $\langle Z^{(l)}\rangle$ and $\langle\Pi^{(l)}\rangle$ for the smallest scale and the change of sign at $l/l_w \cong 0.16$ is similar to the observation reported in previous contributions (see Refs. 12 and 13, among others) as a signature of an inverse energy cascade. The injection scale seems to be $l/l_w \cong 0.16$, a fraction of the inlet barrier, and it remains unchanged in all experiments. Note that the observed dimensions of the initial LAVD patches emitted during the flood phase at the tip of the inlet compare well with the latter estimate.[38] The scale at which we observe the change in sign of $\langle\Pi^{(l)}\rangle$ from negative to positive depends on the experimental parameters and increases with decreasing period T, or wavelength L_s, from about 2 [exp01HR, panel (a)] to about 2.5 [exp04HR, panel (d)].

Finally, we acknowledge some limitations of the present experimental setup in providing information over the full range of scales. In particular, we could not resolve the smallest scales where the energy dissipation occurs, i.e., the Kolmogorov scales that can be estimated as

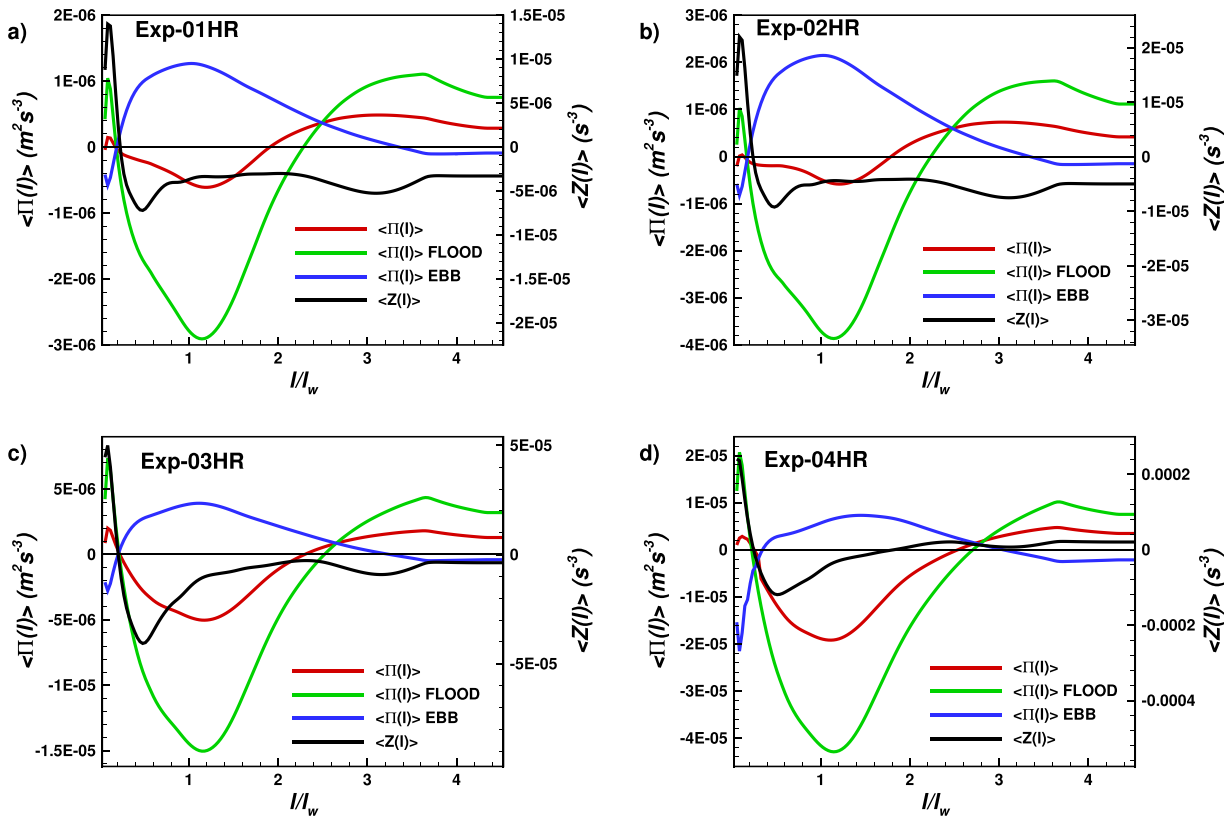

FIG. 4. Time and spatial-averaged $\langle \Pi^{(l)} \rangle$ and $\langle Z^{(l)} \rangle$ for all experiments: (a) experiment 01HR; (b) experiment 02HR; (c) experiment 03HR; and (d) experiment 04HR. The energy fluxes were computed for the flood phase (green line), ebb phase (blue line), and the entire period (red line). The enstrophy transfer rate only averaging over the entire period (black line).

$\eta \sim L/R_e^{3/4}$ (Ref. 65). In the present study, η assumes a value of about 10^{-4} m that is too small compared to the PIV resolution (2 cm). Moreover, the large-scale quadratic dissipation proportional to the drag α is not resolved due to the limitation imposed by the coarse-graining method. In fact, the dissipation due to the drag is linked to the largest flow scale, proportional to the tidal channel length, which cannot be computed using the convolution required by the coarse-graining method. However, we expect that in both limits, where $l/l_w \to 0$ and $l/l_w \to \infty$, the energy transfer should tend to zero, and the results shown in Fig. 4 seem to be in agreement with this behavior.

D. Energy and enstrophy fluxes efficiency

We now investigate the efficiency of the energy and enstrophy transfer using Eqs. (7) and (8). What is important to discuss for understanding the efficiency of the process is the alignment between the eigenframes of the deviatoric part of $\tau_{ij}^{(l)}$ and of the strain rate $S_{ij}^{(l)}$. In fact, we computed the angles $\Theta_\Pi(\boldsymbol{x}, t)$ and $\Theta_Z(\boldsymbol{x}, t)$ for energy and enstrophy, respectively. However, the temporal and spatial variability of the transfer rates require care when these angles are analyzed, since a simple average could hide the details of the process. Following Liao and Ouellette,[14] we started computing the probability density functions (PDFs) of the alignment angles over the domain of interest for all filter scales analyzed and for all time steps within a period.

We report in Figs. 5 and 6 the results obtained for experiments 03HR and 04HR as representative for the entire set of runs. In both figures, the panels from (a1) to (d1) refer to the flood phase of the periodic flow, whereas panels (a2)–(d2) refer to the ebb phase. The PDFs of the angles Θ_Π and Θ_Z are shown in panels (c1) and (d1) (flood phase) and (c2) and (d2) (ebb phase). The PDFs correspond to the distributions for two fixed separations, namely $l/l_w = 0.16$, 1.2 and for prescribed times. Panels (a1) and (b1) report in green the family of curves for $\langle \Pi^{(l)} \rangle$ and $\langle Z^{(l)} \rangle$, respectively, and each line corresponds to a different instant during the flood phase. The specific time at which the PDFs were computed are marked with thick black and blue lines corresponding to the $t = T/8$ (rising flood) and $t = T/4$ (maximum flood). Panels (a2) and (b2) show the same quantities during the ebb phase, and the thick lines correspond to $t = 3T/4$ (maximum ebb) and $t = 7T/8$ (falling ebb). Moreover, the red diamond ($l/l_w = 0.16$) and the black diamonds ($l/l_w = 1.2$) indicate the scale corresponding to the PDFs of panel (c1) and (c2) for the energy angle Θ_Π and of panel (d1) and (d2) for the enstrophy angle Θ_Z. The PDFs of the angles are represented in polar coordinates to help the visualization of the distribution of the values of the angles.

We start discussing the results for experiment 03HR (Fig. 5). During the flood phase [panels (a1)–(d1)], we can observe that for small scales, where $\langle \Pi^{(l)} \rangle 0$ indicating a direct energy transfer toward

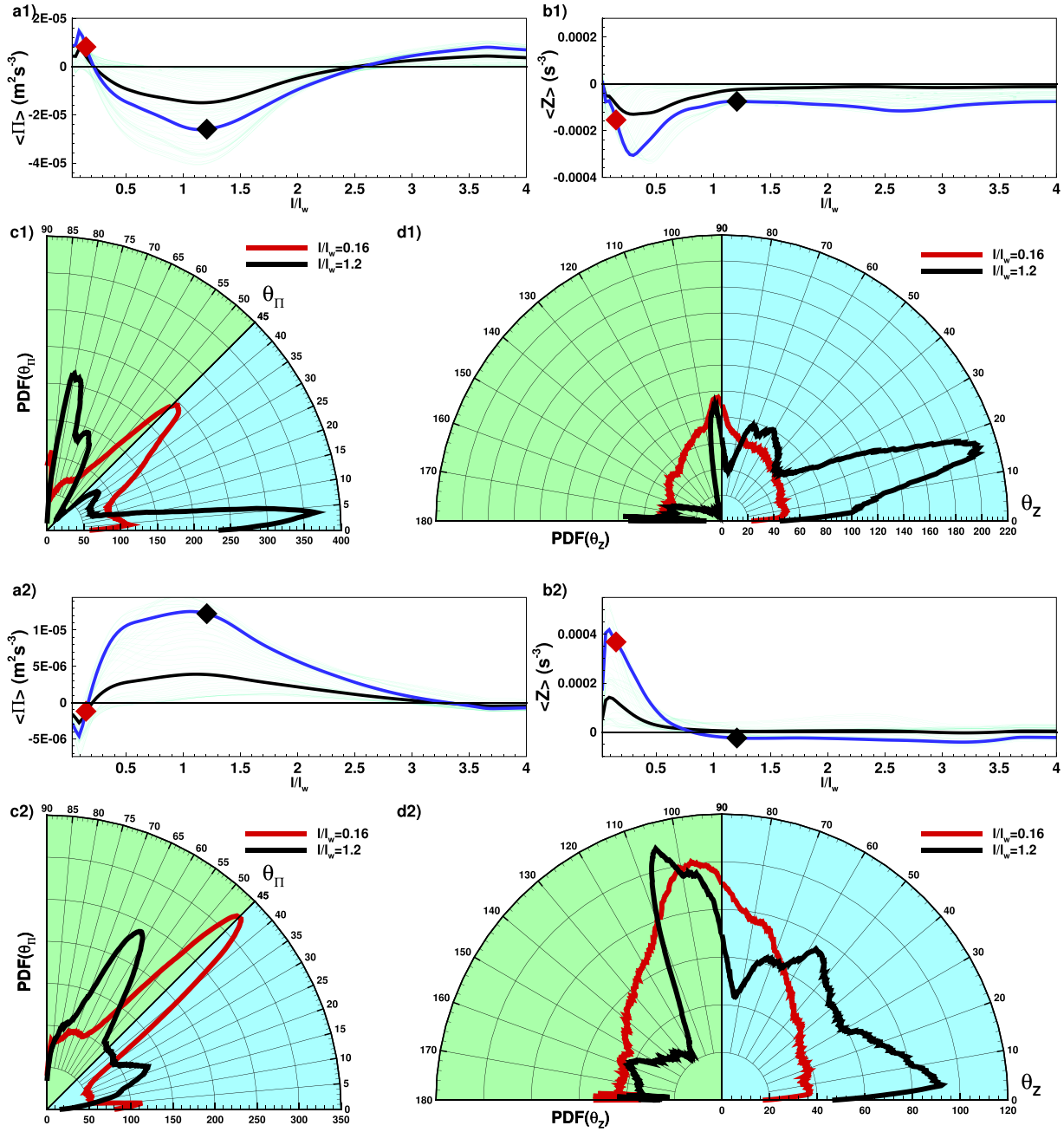

FIG. 5. (a1) $\langle \Pi^{(l)} \rangle$ curves during the flood phase for all time steps (green lines). Blue and black lines indicate two instants, and the corresponding diamonds indicate two selected scales l/l_w for the PDFs of Θ_Π shown in panel (c1); (b1) $\langle Z^{(l)} \rangle$ curves during the flood phase for all time steps (green lines). Blue and black lines indicate two instants, and the corresponding diamonds indicate two selected scales l/l_w for the PDFs of Θ_Z shown in panel (d1). Panels (a2)–(d2) are same as panels (a1)–(d1) during the ebb phase. Data from experiment 03HR ($\epsilon = 0.0225$ and $L_g = 141$ m).

the smaller scales, the PDF of Θ_Π shows a strong peak around 45°, the angle at which the stress and the strain rate are perfectly misaligned, see panel (c1). The PDFs do not show any other strong peak, and this means that for these scale, during the flood phase, direct energy transfer occurs with an extremely low efficiency over the entire domain. For larger scales, we selected the time when the flux is almost minimum [blue line of panel (a1)]. In this case, the PDF shows the strongest peak for $\Theta_\Pi \cong 5°$ that corresponds to an efficiency $\cos(2\Theta_\Pi) \cong 0.98$. Similar results in terms of efficiency are found for the enstrophy fluxes, the PDF of Θ_Z for small-scale enstrophy transfer peaked

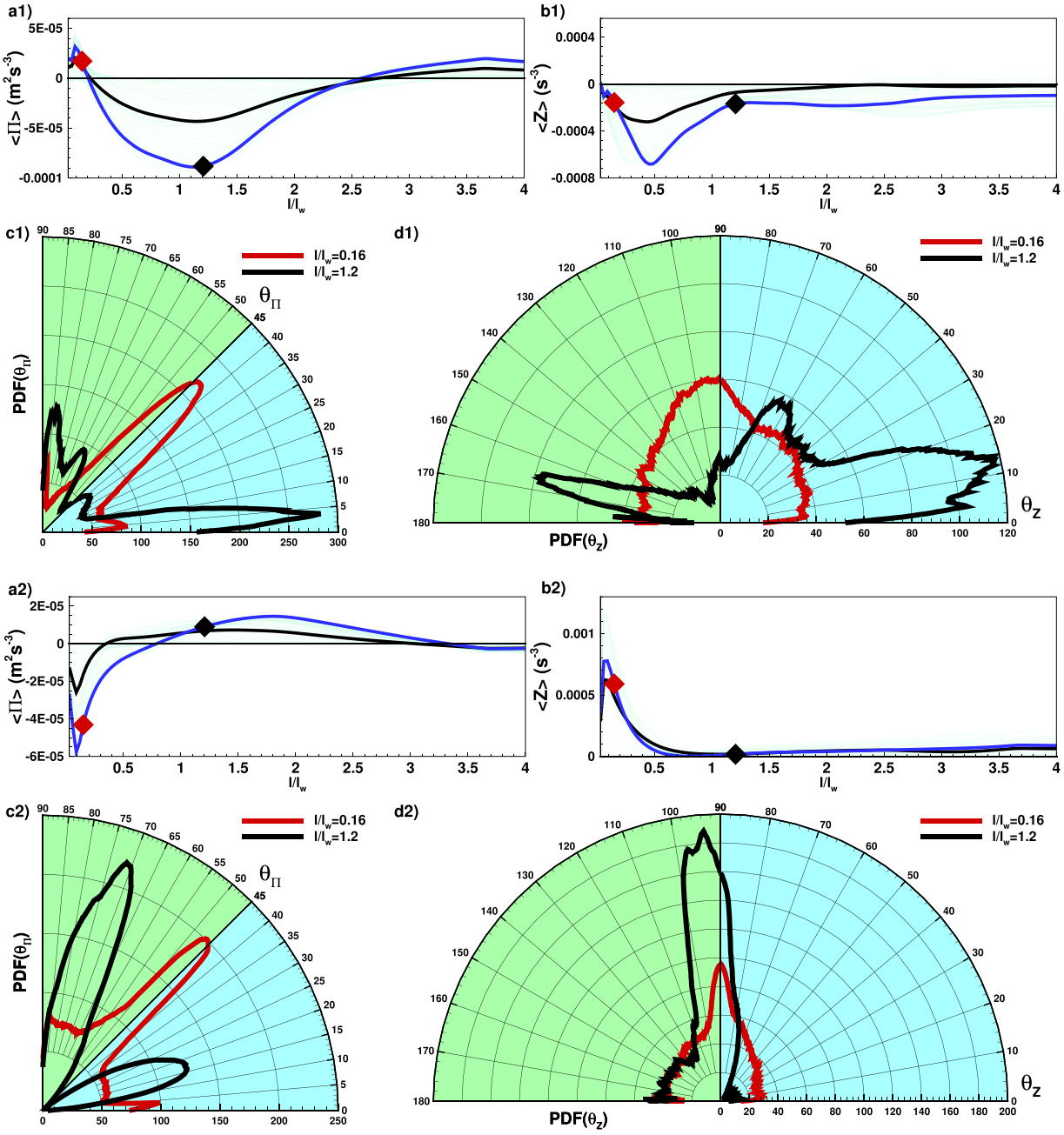

FIG. 6. See caption of Fig. 5. Data from experiment 04HR ($\epsilon = 0.0217$ and $L_g = 108.5$ m).

around the value of 90°. i.e., inefficient transfer. Higher efficiency is found for larger separations, where the enstrophy tends to go toward the larger scales. The ebb phase, panels (a2)–(d2), is characterized by an almost symmetrical behavior compared to the flood phase, as already shown in Fig. 4. The PDF of the alignment angle Θ_Π again peaked around 45° for small scales and, contrary to the flood, shows peak for angles greater than 45° (direct energy cascade). Enstrophy seems to be quite inefficiently transferred for small scales, having peaks around 90°, whereas at larger scales, the PDF shows a broader distribution with the highest peak for $\Theta_Z \cong 105°$. Meanwhile, a large part of the domain exhibits values for the angle Θ_Z between 5° and 55°.

The results for experiment 04HR are shown in Fig. 6. From experiment 03HR to 04HR, the forcing tidal wave has been modified shortening the period and, thus, the wavelength L_g. Qualitatively, the efficiency in the energy transfer remains unchanged compared to experiment 03HR. In fact, small scales are again characterized by an

inefficient transfer, being $\Theta_\Pi \cong 45°$, see panel (c1) and (d1) of Fig. 6. The major differences are found for the PDFs of Θ_Z. Regarding the alignment angle for the enstrophy Θ_Z of experiments 04HR, panels (d1) and (d2), the differences between flood and ebb are remarkable, except for the scales below unity. In fact, the latter are always characterized by an inefficient transfer since the PDFs present a peak around 90°, implying an efficiency around zero, similar to all other experiments. On the contrary, the most pronounced peak during flood is for values around 16°, with a secondary smaller peak for an angle around 165°. In this case, most of the flow domain exhibits a relatively high efficiency transfer to the larger scales. Different from experiment 03HR, we can observe that during the ebb, also scales larger than one show a very narrow distribution for angles slightly higher than 90°. Thus, the direct transfer toward a smaller scale is inefficient for the entire range of separations.

The PDFs in all cases show more than one peak, different from previous observations,[12,15] where the PDFs showed a Gaussian-like distribution. However, the turbulent flow fields of the present case turned out to be strongly inhomogeneous, with the existence of vortical structures not uniformly distributed in space, immersed in a large straining flow with periodic characteristics. This inhomogeneity is responsible for producing non-uniform spatial distributions of $\Pi^{(l)}$ and $Z^{(l)}$, and, eventually, multiple peaks in the PDFs of the alignment between stress and shear rate. Moreover, the periodicity of the flow in response to a variable forcing of slow period is reflected in the periodicity of the transfer rates processes. The time dependence of the alignment angles were recognized to be an important aspect also in other contexts.[9]

Comparing the results obtained for experiments 03HR and 04HR, the tidal period and, consequently, the inviscid wavelength L_g decreases. The distributions of the alignment angles both for energy and enstrophy show a variability in terms of intensities and locations of the main peaks. A major difference can be observed during the ebb phase, where a shorter wavelength (experiment 04HR) tends to produce a narrower distribution of Θ_Z around a value of about 95°, see panel (d2) of Figs. 5 and 6. Regarding the energy, the distribution for $l/l_w = 1.2$ becomes more bimodal in the case of experiment 04HR with two clear peaks. On the contrary, the distributions for the smallest scale shown ($l/l_w = 0.16$) remains more similar, with the only exception of the ebb phase, where, again, the shorter wavelength produces a narrower distribution.

We conclude our analysis considering the overall results in term of the most probable values for the alignments angles Θ_Π and Θ_Z and the corresponding efficiency, namely $\cos(2\Theta_\Pi)$ and $\cos(\Theta_Z)$, to describe the main process over a single period. To take into account the variability of the PDFs, for each time, we selected the angle to the highest peak of the PDFs for each scale l/l_w and then averaging over the tidal period. The results for all experiments are shown in Fig. 7, where the distribution of the angles Θ_Π and Θ_Z over the l/l_w are shown in panels (a) and (b), respectively, and the corresponding efficiency on panels (c) and (d).

Regarding the energy transfer, panels (a) and (c), we can observe that the energy transfer rates for most of the scales is quite inefficient, being the alignment angle in a surrounding of 45°. Only in a range of scales between 1 and 3, the energy efficiency $\cos(2\Theta_\Pi)$ assumes values up to 0.5. This might indicate that over a full period, the inverse energy transfer toward the larger scale is the dominant energy process, whereas the direct energy transfer observed for scale larger than 3 in Fig. 4 is almost inefficient. On the contrary, the overall enstrophy transfer [panels (b) and (d)] is inefficient almost for the entire range of scales.

The physical processes that led to the transition between the cascades observed during the flood and ebb phases were linked to the vortex thinning and strain dominance, respectively.[10,11,37,66] During the

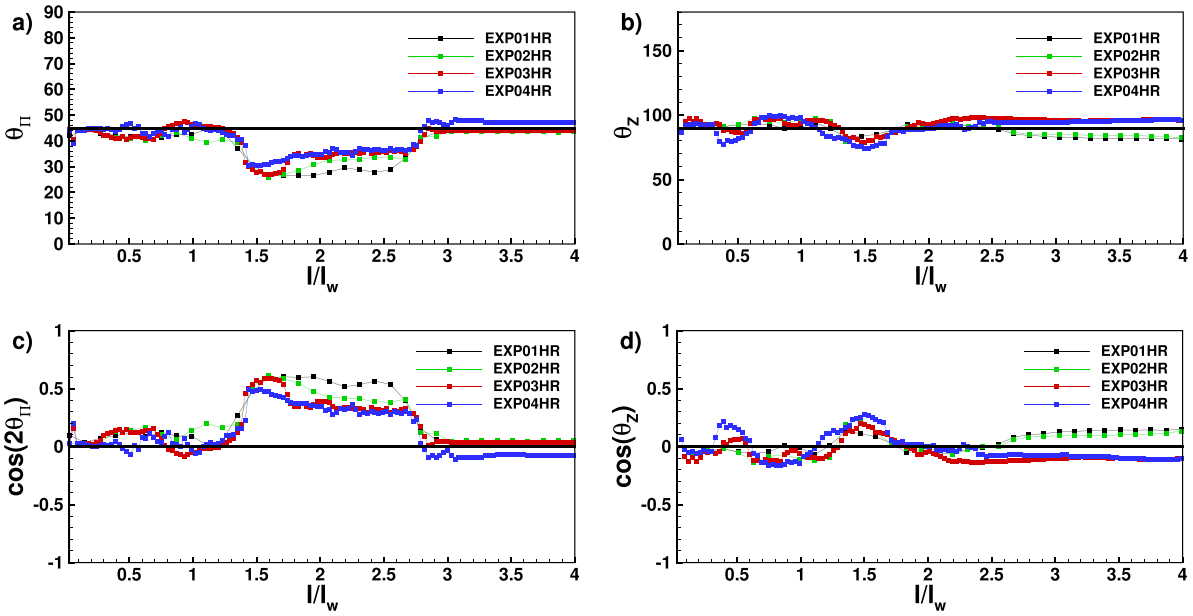

FIG. 7. (a) Mean alignment angles Θ_Π as a function of the scales; (b) mean alignment angles Θ_Z as a function of the scales; (c) mean efficiency $\cos(2\Theta_\Pi)$ as a function of the scales; and (d) mean efficiency $\cos(2\Theta_Z)$ as a function of the scales.

flood phase, the interaction between the vortices shed by the tidal inlet and the mean shear flow deforms the vorticity patches, following the vortex thinning process described in Chen *et al.*[11]

The vortex thinning process during the flood phase in the present experiments is clearly observed from the evolution of LAVD patches as shown in movie 8 (Fig. 8, Multimedia view). The video shows how selected contours of LAVD, identified at the beginning of the flood phase, are advected by the mean flow following the procedure described in Haller *et al.*[50] During the flood, it appears clearly how the LAVD patched tend to shrink along the compressive direction, ultimately leading to a vortex thinning as described in Ref. 11.

On the contrary, the ebb phase is mainly dominated by straining flow region typically associated with a direct energy cascade.

We are aware that the mechanisms introduced by Chen *et al.*[11] and Xiao *et al.*[12] do not necessarily imply the presence of coherent vortices, but rather the thinning mechanism is linked to deformation of the vorticity fields due to large-scale strain. The computation and advection of LAVD fields do indeed suggest the presence of a similar mechanism. Moreover, relevant for the present discussion could be the role of flow inhomogeneity and/or the presence of coherent flow structures as a possible mechanism for sustaining energy transfers through the flow scales even for Reynolds numbers much lower than the ones required by the Kolmogorov's theory.[67–69] It is reasonable to argue that in the present case, both mechanisms play a role in the establishment of the observed direct and indirect energy cascade.

Regarding the efficiency of the processes, the present results are slightly different from previous studies. The overall efficiency of the energy transfers where an inverse energy cascade is observed, e.g., in the study by Fang and Ouellette,[9] has been found to be quite weak for the entire range of scales, though slightly higher where there is net inverse energy transfer. An established view of the overall energy cascade in turbulence describes the process as a result of a weak asymmetry between locally strong forward and inverse transfer events.[11,43] Fang and Ouellette[9] ascribed the low efficiency to the effect of advection that interferes with the delicate process of alignments between stress and strain. In the present case, the large-scale advection is a periodical flow that, however, seems to not generate misalignment between the stress and the strain rate. In the present case, the direct energy part of the process is indeed rather inefficient, Θ_Π is almost always 45°, i.e., the angle at which the stress and the strain rate are perfectly misaligned. However, the efficiency is quite high in the range of scale where the overall process is dominated by an inverse energy cascade. A comprehensive analysis of the evolution of the vortical structure of the present tidal flows showed the details of the vortex shedding and the consequent thinning process.[38] The LAVD field evolution showed how the initial vortex remained embedded in a coherent strain field long enough for the thinning process to occur, and, thus, governing an efficient inverse energy cascade.

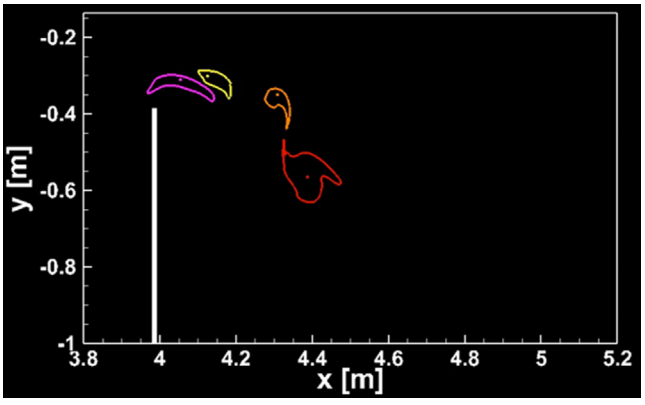

FIG. 8. Snapshot of the time evolution of selected contours of LAVD advected following Haller *et al.*[50] The LAVD contours were selected out of the computation of the LAVD fields shown in movie 8. Multimedia view: https://doi.org/10.1063/5.0142848.2

IV. CONCLUSIONS

We reported the results obtained from a detailed analysis of energy and enstrophy transfer rates associated with a case of periodic flows, which are of considerable importance in the field of geophysical fluid dynamics. Periodical flows were generated in a large-scale tidal flume, and time resolved high-resolution velocity fields were measured using particle image velocimetry. We applied a coarse-grain technique that is considered one of the most powerful frameworks to understand the energy and enstrophy transfers among the different flow scales. The results suggested that the energy and enstrophy fluxes maintained a strong variability in space and time. Depending on the phase of the periodical flow, the energy/enstrophy processes could exhibit both direct and inverse energy cascades. Transitions appear smooth in time between the different scenarios, with no abrupt changes. From a physical standpoint, the inverse energy cascade was associated with the vortex shedding at the inlet and the subsequent thinning and merging into larger vortical structures. The overall process on a single period showed multiple energy and enstrophy cascades depending on the range of scales considered. The computation of the alignment angle between the eigenframes of the stress and large-scale strain rate indicated that the most efficient process was the inverse energy cascade from the injection scale to a scale comparable with the lager vortical structures. The process was found to be inefficient for every scale where a direct cascade occurred. Enstrophy transfers seem to be, on average, much less efficient compared to the energy transfers. Finally, the results of the present study represent a step forward in understanding the energy processes that occur in geophysical flows, typical of the coastal areas and estuarine environment, where the interaction between the tidal current (one of the main agents of transport) interacts with the complex geometry of the shores. Tides are often well described by a dominant harmonic, typically the lunar semi-diurnal, and, in this sense, our results are relevant although the tidal wave has been represented with a single harmonic. Future investigations will be devoted to studying the interaction of the tidal current with a uniform flow representing a possible river input.

ACKNOWLEDGMENTS

The research has been conducted without any external funding.

AUTHOR DECLARATIONS

Conflict of Interest

The authors have no conflicts to disclose.

Author Contributions

Annalisa De Leo: Conceptualization (equal); Data curation (equal); Formal analysis (equal); Investigation (equal); Methodology (equal); Validation (equal); Writing – original draft (equal); Writing – review & editing (equal). **Alessandro Stocchino:** Conceptualization (equal); Data curation (equal); Formal analysis (equal); Investigation (equal); Methodology (equal); Validation (equal); Writing – original draft (equal); Writing – review & editing (equal).

DATA AVAILABILITY

The data that support the findings of this study are available from the corresponding author upon reasonable request.

REFERENCES

[1]A. Alexakis and L. Biferale, "Cascades and transitions in turbulent flows," Phys. Rep. **767–769**, 1–101 (2018).
[2]F. Thiesset and L. Danaila, "The illusion of a Kolmogorov cascade," J. Fluid Mech. **902**, F1 (2020).
[3]M. Germano, "Turbulence: The filtering approach," J. Fluid Mech. **238**, 325–336 (1992).
[4]S. Liu, C. Meneveau, and J. Katz, "On the properties of similarity subgrid-scale models as deduced from measurements in a turbulent jet," J. Fluid Mech. **275**, 83–119 (1994).
[5]H. Aluie, M. Hecht, and G. K. Vallis, "Mapping the energy cascade in the North Atlantic Ocean: The coarse-graining approach," J. Phys. Oceanogr. **48**, 225–244 (2018).
[6]G. L. Eyink, "Exact results on scaling exponents in the 2D enstrophy cascade," Phys. Rev. Lett. **74**, 3800 (1995).
[7]H. Aluie and G. L. Eyink, "Localness of energy cascade in hydrodynamic turbulence—II: Sharp spectral filter," Phys. Fluids **21**, 115108 (2009).
[8]G. L. Eyink and H. Aluie, "Localness of energy cascade in hydrodynamic turbulence—I: Smooth coarse graining," Phys. Fluids **21**, 115107 (2009).
[9]L. Fang and N. T. Ouellette, "Advection and the efficiency of spectral energy transfer in two-dimensional turbulence," Phys. Rev. Lett. **117**, 104501 (2016).
[10]S. Chen, R. E. Ecke, G. L. Eyink, X. Wang, and Z. Xiao, "Physical mechanism of the two-dimensional enstrophy cascade," Phys. Rev. Lett. **91**, 214501 (2003).
[11]S. Chen, R. E. Ecke, G. L. Eyink, M. Rivera, M. Wan, and Z. Xiao, "Physical mechanism of the two-dimensional inverse energy cascade," Phys. Rev. Lett. **96**, 084502 (2006).
[12]Z. Xiao, M. Wan, S. Chen, and G. Eyink, "Physical mechanism of the inverse energy cascade of two-dimensional turbulence: A numerical investigation," J. Fluid Mech. **619**, 1–44 (2009).
[13]D. H. Kelley and N. T. Ouellette, "Spatiotemporal persistence of spectral fluxes in two-dimensional weak turbulence," Phys. Fluids **23**, 115101 (2011).
[14]Y. Liao and N. T. Ouellette, "Spatial structure of spectral transport in two-dimensional flow," J. Fluid Mech. **725**, 281–298 (2013).
[15]Y. Liao and N. T. Ouellette, "Geometry of scale-to-scale energy and enstrophy transport in two-dimensional flow," Phys. Fluids **26**, 045103 (2014).
[16]M. Rivera, H. Aluie, and R. Ecke, "The direct enstrophy cascade of two-dimensional soap film flows," Phys. Fluids **26**, 055105 (2014).
[17]S. J. Benavides and A. Alexakis, "Critical transitions in thin layer turbulence," J. Fluid Mech. **822**, 364–385 (2017).
[18]J. G. Ballouz, P. L. Johnson, and N. T. Ouellette, "Temporal dynamics of the alignment of the turbulent stress and strain rate," Phys. Rev. Fluids **5**, 114606 (2020).
[19]R. B. Scott and F. Wang, "Direct evidence of an oceanic inverse kinetic energy cascade from satellite altimetry," J. Phys. Oceanogr. **35**, 1650–1666 (2005).
[20]A. C. Poje, T. M. Özgökmen, D. J. Bogucki, and A. Kirwan, "Evidence of a forward energy cascade and Kolmogorov self-similarity in submesoscale ocean surface drifter observations," Phys. Fluids **29**, 020701 (2017).
[21]A. C. Savage, B. K. Arbic, J. G. Richman, J. F. Shriver, M. H. Alford, M. C. Buijsman, J. T. Farrar, H. Sharma, G. Voet, A. J. Wallcraft *et al.*, "Frequency content of sea surface height variability from internal gravity waves to mesoscale eddies," J. Geophys. Res. **122**, 2519–2538, https://doi.org/10.1002/2016JC012331 (2017).
[22]H. Khatri, J. Sukhatme, A. Kumar, and M. K. Verma, "Surface ocean enstrophy, kinetic energy fluxes, and spectra from satellite altimetry," J. Geophys. Res. **123**, 3875–3892, https://doi.org/10.1029/2017JC013516 (2018).
[23]H. S. Torres, P. Klein, D. Menemenlis, B. Qiu, Z. Su, J. Wang, S. Chen, and L.-L. Fu, "Partitioning ocean motions into balanced motions and internal gravity waves: A modeling study in anticipation of future space missions," J. Geophys. Res. **123**, 8084–8105, https://doi.org/10.1029/2018JC014438 (2018).
[24]S. M. Kelly, J. D. Nash, K. I. Martini, M. H. Alford, and E. Kunze, "The cascade of tidal energy from low to high modes on a continental slope," J. Phys. Oceanogr. **42**, 1217–1232 (2012).
[25]F. Nicolau del Roure, S. A. Socolofsky, and K.-A. Chang, "Structure and evolution of tidal starting jet vortices at idealized barotropic inlets," J. Geophys. Res. **114**, C05024, https://doi.org/10.1029/2008JC004997 (2009).
[26]P. MacCready and W. R. Geyer, "Advances in estuarine physics," Annu. Rev. Mar. Sci. **2**, 35–58 (2010).
[27]K. A. Whilden, S. A. Socolofsky, K.-A. Chang, and J. L. Irish, "Using surface drifter observations to measure tidal vortices and relative diffusion at Aransas Pass, Texas," Environ. Fluid Mech. **14**, 1147–1172 (2014).
[28]W. R. Geyer and P. MacCready, "The estuarine circulation," Annu. Rev. Fluid Mech. **46**, 175–197 (2014).
[29]K. Suara, H. Chanson, M. Borgas, and R. J. Brown, "Relative dispersion of clustered drifters in a small micro-tidal estuary," Estuarine, Coastal Shelf Sci. **194**, 1–15 (2017).
[30]F. Enrile, G. Besio, A. Stocchino, M. Magaldi, C. Mantovani, S. Cosoli, R. Gerin, and P. Poulain, "Evaluation of surface Lagrangian transport barriers in the Gulf of Trieste," Cont. Shelf Res. **167**, 125–138 (2018).
[31]F. Enrile, G. Besio, A. Stocchino, and M. G. Magaldi, "Influence of initial conditions on absolute and relative dispersion in semi-enclosed basins," PloS One **14**, e0221009 (2019).
[32]P. Blondeaux and G. Vittori, "Modeling transverse coastal bedforms at Anna Maria Island (Florida)," J. Geophys. Res. **125**, e2019JC015837, https://doi.org/10.1029/2019JC015837 (2020).
[33]I. Zhabin and N. Luk'yanova, "Sub-mesoscale vortex streets in the region of the Shantar Islands (Sea of Okhotsk), according to satellite remote sensing data," Izv., Atmos. Oceanic Phys. **56**, 1615–1620 (2020).
[34]C. He, Z.-Y. Yin, A. Stocchino, O. W. H. Wai, and S. Li, "The coastal macrovortices dynamics in Hong Kong waters and its impact on water quality," Ocean Modell. **175**, 102034 (2022).
[35]C. V. Vouriot, A. Angeloudis, S. C. Kramer, and M. D. Piggott, "Fate of large-scale vortices in idealized tidal lagoons," Environ. Fluid Mech. **19**, 329–348 (2019).
[36]O. A. Nøst and E. Børve, "Flow separation, dipole formation, and water exchange through tidal straits," Ocean Sci. **17**, 1403–1420 (2021).
[37]A. De Leo and A. Stocchino, "Evidence of transient energy and enstrophy cascades in tidal flows: A scale to scale analysis," Geophys. Res. Lett. **49**, e2022GL098043, https://doi.org/10.1029/2022GL098043 (2022).
[38]A. De Leo, F. Enrile, and A. Stocchino, "Periodic Lagrangian coherent structures around a tidal inlet," Front. Mar. Sci. **9**, 1472 (2022).
[39]A. De Leo, N. Tambroni, and A. Stocchino, "Dispersion processes in weakly dissipative tidal channels," J. Geophys. Res. **127**, e2021JC018315, https://doi.org/10.1029/2021JC0183152 (2022).
[40]M. Toffolon, G. Vignoli, and M. Tubino, "Relevant parameters and finite amplitude effects in estuarine hydrodynamics," J. Geophys. Res. **111**, C10014, https://doi.org/10.1029/2005JC003104 (2006).
[41]R. Adrian, "Dynamic ranges of velocity and spatial resolution of particle image velocimetry," Meas. Sci. Technol. **8**, 1393 (1997).
[42]R. J. Adrian, "Twenty years of particle image velocimetry," Exp. Fluids **39**, 159–169 (2005).
[43]M. Rivera, W. Daniel, S. Chen, and R. Ecke, "Energy and enstrophy transfer in decaying two-dimensional turbulence," Phys. Rev. Lett. **90**, 104502 (2003).
[44]J. G. Ballouz and N. T. Ouellette, "Tensor geometry in the turbulent cascade," J. Fluid Mech. **835**, 1048–1064 (2018).
[45]L. Fang, S. Balasuriya, and N. T. Ouellette, "Local linearity, coherent structures, and scale-to-scale coupling in turbulent flow," Phys. Rev. Fluids **4**, 014501 (2019).

[46]L. Siegelman, P. Klein, A. P. Ingersoll, S. P. Ewald, W. R. Young, A. Bracco, A. Mura, A. Adriani, D. Grassi, C. Plainaki *et al.*, "Moist convection drives an upscale energy transfer at Jovian high latitudes," Nat. Phys. **18**, 357–361 (2022).
[47]A. Tsinober, *An Informal Introduction to Turbulence* (Springer Science & Business Media, 2001), Vol. 63.
[48]P. Tabeling, "Two-dimensional turbulence: A physicist approach," Phys. Rep. **362**, 1–62 (2002).
[49]G. Boffetta and R. E. Ecke, "Two-dimensional turbulence," Annu. Rev. Fluid Mech. **44**, 427–451 (2012).
[50]G. Haller, A. Hadjighasem, M. Farazmand, and F. Huhn, "Defining coherent vortices objectively from the vorticity," J. Fluid Mech. **795**, 136–173 (2016).
[51]S. C. Shadden, F. Lekien, and J. E. Marsden, "Definition and properties of Lagrangian coherent structures from finite-time Lyapunov exponents in two-dimensional aperiodic flows," Physica D **212**, 271–304 (2005).
[52]W. Tang, M. Mathur, G. Haller, D. C. Hahn, and F. H. Ruggiero, "Lagrangian coherent structures near a subtropical jet stream," J. Atmos. Sci. **67**, 2307–2319 (2010).
[53]G. Haller and F. J. Beron-Vera, "Geodesic theory of transport barriers in two-dimensional flows," Physica D **241**, 1680–1702 (2012).
[54]G. Haller, "Lagrangian coherent structures," Annu. Rev. Fluid Mech. **47**, 137–162 (2015).
[55]I. Nezu, K. Onitsuka, and K. Iketani, "Coherent horizontal vortices in compound open-channel flows," in *Hydraulic Modeling*, edited by V. P. Singh, I. W Seo, and J. H. Sonu (Water Resources Publication, 1999), pp. 17–32.
[56]K. Shiono and D. W. Knight, "Turbulent open-channel flows with variable depth across the channel," J. Fluid Mech. **222**, 617–646 (1991).
[57]V. Nikora, R. Nokes, W. Veale, M. Davidson, and G. Jirka, "Large-scale turbulent structure of uniform shallow free-surface flows," Environ. Fluid Mech. **7**, 159–172 (2007).
[58]A. Stocchino and M. Brocchini, "Horizontal mixing of quasi-uniform, straight, compound channel flows," J. Fluid Mech. **643**, 425–435 (2010).
[59]A. Stocchino, G. Besio, S. Angiolani, and M. Brocchini, "Lagrangian mixing in straight compound channels," J. Fluid Mech. **675**, 168–198 (2011).
[60]G. Besio, A. Stocchino, S. Angiolani, and M. Brocchini, "Transversal and longitudinal mixing in compound channels," Water Resour. Res. **48**, W12517, https://doi.org/10.1029/2012WR012316 (2012).
[61]F. Enrile, G. Besio, and A. Stocchino, "Shear and shearless Lagrangian structures in compound channels," Adv. Water Resour. **113**, 141–154 (2018).
[62]S. Proust, C. Berni, and V. I. Nikora, "Shallow mixing layers over hydraulically smooth bottom in a tilted open channel," J. Fluid Mech. **951**, A17 (2022).
[63]J. Zhou, R. J. Adrian, S. Balachandar, and T. Kendall, "Mechanisms for generating coherent packets of hairpin vortices in channel flow," J. Fluid Mech. **387**, 353–396 (1999).
[64]G. Boffetta and S. Musacchio, "Evidence for the double cascade scenario in two-dimensional turbulence," Phys. Rev. E **82**, 016307 (2010).
[65]H. Tennekes, J. L. Lumley, J. L. Lumley *et al.*, *A First Course in Turbulence* (MIT Press, 1972).
[66]W. Wang, C. Pan, and J. Wang, "Energy transfer structures associated with large-scale motions in a turbulent boundary layer," J. Fluid Mech. **906**, A14 (2021).
[67]F. Thiesset, R. Antonia, and L. Danaila, "Scale-by-scale turbulent energy budget in the intermediate wake of two-dimensional generators," Phys. Fluids **25**, 115105 (2013).
[68]F. Thiesset, L. Danaila, and R. Antonia, "Dynamical interactions between the coherent motion and small scales in a cylinder wake," J. Fluid Mech. **749**, 201–226 (2014).
[69]F. A. Portela, G. Papadakis, and J. Vassilicos, "The role of coherent structures and inhomogeneity in near-field interscale turbulent energy transfers," J. Fluid Mech. **896**, A16 (2020).